RSC Advances

ROYAL SOCIETY OF CHEMISTRY

PAPER

View Article Online
View Journal | View Issue

Check for updates

Cite this: *RSC Adv.*, 2025, **15**, 34754

Catalytic conversion of cellulose to ethylene glycol using functionalized covalent organic frameworks

Yu Zhao,†[a] Yuan Ju,†[a] Baozhen Guo,[a] Peng Gan,*[ab] Pengfei Lv, *[c] Jingli Yang,[a] Chengcheng Qiao[a] and Kai Zhang *[a]

Received 17th July 2025
Accepted 12th September 2025

DOI: 10.1039/d5ra05136c

rsc.li/rsc-advances

The utilization of abundant and renewable cellulose as an alternative to fossil resources provides a promising pathway for the sustainable production of bio-based chemicals. The development of multifunctional catalysts is key to achieving the efficient conversion of cellulose into high value-added chemicals. In this study, a combination of *in situ* and post-synthetic strategies was employed to synthesize functionalized covalent organic frameworks (COFs). Using aldehyde monomers containing phenolic hydroxyl groups and amine monomers with triazine structure as raw materials, COFs (TATP) rich in acidic active sites were successfully synthesized *via* the solvothermal method. Subsequently, a multifunctional catalyst (Ru-WO_x/TATP) capable of catalyzing hydrolysis, hydrogenolysis, and hydrogenation reactions was developed by loading active metals ruthenium (Ru) and tungsten (W). Finally, this catalyst was applied to the research on one-step catalytic conversion of cellulose to ethylene glycol (EG). The results showed that Ru–WO_x/TATP exhibited good crystallinity and thermal stability, and showed excellent catalytic performance and high selectivity for EG in the one-pot aqueous-phase conversion of cellulose. Under the optimal reaction conditions of 245 °C, an initial hydrogen pressure of 5 MPa, a substrate concentration of 1%, and a reaction time of 3 h, complete cellulose conversion was achieved, with an ethylene glycol yield of up to 62.9%. This work innovatively developed a functionalized COF with catalytic capabilities for hydrolysis, hydrogenolysis, and hydrogenation, and applied it to the catalytic conversion of cellulose into EG, thereby expanding the application scope of COFs in biomass catalysis.

1. Introduction

With the growing severity of the global energy crisis and environmental issues, the development and utilization of renewable energy sources have attracted widespread attention.[1] In recent years, the conversion of lignocellulosic biomass components into high value-added chemicals or fuels has emerged as a research hotspot.[2,3] Among these components, cellulose is considered a particularly promising biomass resource for replacing fossil feedstocks due to its abundance, wide distribution, and renewability.[4,5] Cellulose is a linear polymer composed of D-glucose units linked by β-1,4-glycosidic bonds. Its high oxygen-to-carbon ratio makes it suitable for the production of low-carbon polyols such as ethylene glycol and propylene glycol through catalytic conversion, offering high atom economy.[6–8] Ethylene glycol (EG), a key bulk chemical, is widely used in the synthesis of chemical intermediates such as EG ethers and glyoxal, and in the production of polyesters, antifreeze agents, and lubricants.[9] Among these applications, polyesters serve as the fundamental raw materials for producing polyester fibers, which are vital to the synthetic fiber industry.[10] As a major producer of synthetic fibers, China faces a domestic shortage of EG, with production failing to meet the strong market demand, resulting in a heavy reliance on imports. Currently, EG is primarily derived from petrochemical resources.[11–13] However, the gradual depletion of fossil resources is expected to significantly impact its supply. Therefore, the development of sustainable processes for EG production has become an urgent need.

Bifunctional catalysts mediate sequential or parallel reactions by integrating multiple active sites, which effectively overcomes these challenges. They not only eliminate the need for separate process steps but also enhance reaction selectivity through optimizing the synergy between catalytic functions. The efficiency of bifunctional catalysts stems from the interaction between two or more active components, typically

---

[a] *State Key Laboratory of Biobased Materials and Green Papermaking, State Key Laboratory of Green Papermaking and Resource Recycling, Qilu University of Technology (Shandong Academy of Sciences), Jinan 250353, China. E-mail: ganpdyx@163.com; zhangkai2018@qlu.edu.cn*

[b] *Key Laboratory of Clean Pulp & Papermaking and Pollution Control of Guangxi, College of Light Industrial and Food Engineering, Guangxi University, Nanning 530004, China*

[c] *Key Laboratory of Eco-textiles, Ministry of Education, Jiangnan University, Wuxi, 214122, P. R. China. E-mail: pengfeilv@jiangnan.edu.cn*

† Yu Zhao and Yuan Ju contributed equally to this work.

combining metal sites with acid/base sites. This integration is crucial in biomass conversion; for instance, the process of cellulose hydrolysis-hydrogenation to EG involves three key steps: (i) acid-catalyzed hydrolysis of cellulose to glucose; (ii) cleavage of carbon–carbon bonds in glucose *via* retro-aldol condensation (RAC) to generate glycolaldehyde; (iii) hydrogenation of glycolaldehyde to produce ethylene glycol.[14–16] Ji *et al.* first synthesized a Ni–W_2C/AC catalyst *via* a carbothermal reduction method, using activated carbon as the support. This catalyst achieved complete cellulose conversion within 30 min, with an EG yield of 61%. The study revealed that the weak adsorption of EG molecules on the Ni-modified W_2C surface played a key role in enhancing product selectivity. This work marked the first highly selective conversion of cellulose to EG, offering a new strategy for the efficient production of high-value chemicals from biomass.[17] Subsequently, Zhang *et al.* developed a Ru–$W_{18}O_{49}$/RGO catalyst *via* a solvothermal reduction method under mild conditions, using graphene oxide as the support. Structural characterizations indicated that the catalyst consisted of ultrathin graphene nanosheets loaded with Ru nanoparticles and densely distributed $W_{18}O_{49}$ nanowires. This two-dimensional heterostructure provided abundant active sites for the selective conversion of cellulose to EG. Under reaction conditions of 245 °C and 60 min, the cellulose conversion reached 100%, and the EG yield was 62.5%. This study introduced a facile and mild approach to preparing bimetallic catalysts with high efficiency.[18] Carbon nanotubes (CNTs) have been proven to be excellent supports for Ni–W catalysts. Xiao *et al.* utilized 15% Ni–20% W/CNT to convert cellulose into EG at 240 °C, achieving a yield of 55%. This performance is attributed to the large mesoporous structure of CNTs, which facilitates mass transfer and suppresses metal agglomeration.[19] Notably, Ribeiro *et al.* further optimized the Ni–W/CNT system by regulating the metal ratio, achieving an EG yield of >50% under milder conditions (205 °C, 50 bar H_2). Moreover, the catalyst remained stable after 6 cycles. This advancement highlights the significance of the interaction between the support and active sites.[20] In summary, the use of porous materials as supports for the dispersion of metal active sites enables the design of multifunctional catalysts with hydrolysis, hydrogenolysis, and hydrogenation capabilities. Such catalysts not only facilitate the efficient conversion of cellulose but also ensure high yields of EG.

Covalent organic frameworks (COFs) are crystalline porous materials constructed from organic building blocks interconnected through covalent bonds. These organic units, typically composed of light elements such as carbon, hydrogen, oxygen, boron, and nitrogen, can extend in two or three dimensions to form robust organic frameworks.[21] Due to their high specific surface area, tunable pore structures, excellent chemical stability, and ease of functional modification, COFs have demonstrated great application potential in various fields including catalysis, gas and energy storage, sensing, electronic devices, and drug delivery.[22] In particular, COFs have emerged as promising candidates in catalysis owing to their structural tunability, ease of functional design, and outstanding reusability.[23,24] For instance, Artz *et al.* developed a Ru-loaded covalent triazine framework (Ru/CTF), which exhibited excellent catalytic activity and stability in the oxidation of 5-hydroxymethylfurfural to produce furan dicarboxylic acid and furan dialdehyde.[25] In recent work by our group, a functionalized COF (TAPT–DHPA) was synthesized using tris(4-aminophenyl)-1,3,5-triazine and 2,5-dihydroxyterephthalaldehyde as monomers. The ionization of phenolic hydroxyl groups and the electron-withdrawing effect of the triazine rings endowed the material with abundant acidic sites. The catalyst exhibited excellent performance in the liquid-phase catalytic conversion of pentose to furfural, achieving a furfural yield of up to 86.7% with a catalyst loading as low as 0.33 wt%.[26]

In summary, COFs hold significant promise as catalysts for the valorization of biomass into high value-added chemicals. Hence, the present study integrates both *in situ* synthesis and post-synthetic modification strategies to prepare COFs enriched with acidic sites. Ru and W were subsequently loaded onto the COFs to construct multifunctional composite catalysts. These catalysts were applied to the one-pot aqueous-phase catalytic conversion of cellulose into EG, aiming to expand the diversity of multifunctional catalysts in this field and broaden the application scope of functionalized COFs in biomass conversion.

2. Materials and methods

2.1 Materials and chemicals

n-Butanol (*n*-BuOH), *o*-dichlorobenzene (*o*-DCB), *N*,*N*-dimethylformamide (DMF), tetrahydrofuran (THF), acetone, glacial acetic acid (AcOH), and ethylene glycol (EG) were all purchased from Aladdin Reagent Co., Ltd (Shanghai, China). 4,4′,4″-(1,3,5-Triazine-2,4,6-triyl)trianiline (TA), 1,3,5-triformylphloroglucinol (TP), 1,3,5-tris(4-aminophenyl)benzene (TB) and benzene-1,3,5-tricarbaldehyde (BT) were obtained from Shanghai Macklin Biochemical Co., Ltd. Microcrystalline cellulose was supplied by Beijing InnoChem Science & Technology Co., Ltd. Tungsten(VI) chloride (WCl_6, 99.9%) and ruthenium(III) chloride hydrate ($RuCl_3 \cdot nH_2O$, Ru content 38%) were provided by Shanghai Bok Chemical Technology Co., Ltd. High-purity hydrogen gas was purchased from Jinan Deyang Gas Co., Ltd.

2.2 Synthesis of COFs

To a 10 mL pressure-resistant vial, 170.13 mg of TA and 119.6 mg of TP were added, followed by 6.6 mL of a mixed solvent consisting of *n*-BuOH, *o*-DCB and AcOH in a volume ratio of 5 : 5 : 1. The mixture was ultrasonicated for 20 min to ensure complete dissolution. The vial was then rapidly frozen in a liquid nitrogen bath at 77 K. A degassing process was carried out by performing three freeze–pump–thaw cycles. After degassing, the vial was sealed under vacuum and heated at 120 °C for 72 h. Upon completion of the reaction, the resulting yellow precipitate was collected by vacuum filtration, followed by successive washing with DMF, tetrahydrofuran, acetone, and deionized water. The product was then dried under vacuum at 80 °C overnight to afford the TATP material, with a yield exceeding 95%. The synthesis of TBBT, TBTP, and TABT was performed following the same procedure as that of TATP.

2.3 Preparation of functionalized COF composite materials

The functionalized COFs composite materials were prepared following a previously reported method.[26] First, 0.2 g of TATP and 0.026 g of ruthenium(III) chloride hydrate were accurately weighed and dispersed in 30 mL of deionized water with thorough stirring. Separately, tungsten(VI) chloride was dissolved in 40 mL of EG and sonicated for 30 min, followed by magnetic stirring until a clear and colorless solution was obtained. Under vigorous stirring, the EG solution was slowly added dropwise into the aqueous dispersion. The resulting mixture was then transferred into a Teflon-lined autoclave and heated at 210 °C for 4 h in a convection oven. After the reaction, the autoclave was allowed to cool to room temperature, and the solid product was collected by filtration. The catalyst was washed several times with distilled water by vacuum filtration. Finally, the resulting Ru–WO_x/TATP composite was dried under vacuum at 80 °C overnight. The control samples, including Ru/TATP, WO_x/TATP, as well as Ru–WO_x/TBBT, Ru–WO_x/TBTP, and Ru–WO_x/TABT, were prepared using the same procedure.

2.4 Characterization of the synthesized materials

X-ray diffraction (XRD) patterns were recorded using a D8 ADVANCE diffractometer (Bruker) equipped with a Cu Kα radiation source ($\lambda = 0.15418$ nm) under operating conditions of 40 kV and 40 mA. The data were collected with a step size of 0.02° and a scanning rate of 0.1 s per step. X-ray photoelectron spectroscopy (XPS) was performed on an ESCALAB 250 Xi spectrometer (Thermo Scientific) using a non-monochromatic Al Kα radiation source. Nitrogen adsorption–desorption isotherms were measured at 77 K using a Micromeritics ASAP 2010 instrument. Prior to analysis, the samples were degassed at 523 K for 5 h. The morphology and elemental composition of the materials were examined using a scanning electron microscope (SEM, Merlin, Zeiss) equipped with an energy-dispersive X-ray spectroscopy detector (EDX, X-MaxN 20), and a transmission electron microscope (TEM, JEM-2100F, JEOL) equipped with a field emission gun (FEG) and an X-ray analysis system.

2.5 Catalytic reaction and product analysis

The catalytic reaction was carried out in a 100 mL stainless-steel high-pressure reactor (Parr 5100 HP) by charging the catalyst, 50 mL of water, and 0.5 g of microcrystalline cellulose. The reactor was purged with hydrogen gas 5–8 times at atmospheric pressure to remove air, followed by pressurization to 5 MPa with hydrogen. After sealing, the reaction mixture was heated to 245 °C and stirred at a constant speed of 1000 rpm for a set period of time. Upon completion, the reactor was cooled to room temperature. The liquid products were collected by filtration through a microporous membrane with an average pore size of 0.45 μm. The composition of the liquid phase was analyzed using high-performance liquid chromatography (HPLC, Waters e2695) equipped with a refractive index detector and a Shodex SC 100 column. The detection conditions were as follows: the mobile phase was ultrapure water with a flow rate of 0.6 mL min^{-1}; the column temperature and detector temperature were 75 °C and 50 °C, respectively; and the injection volume was 20 μL. The internal standard method was used to determine the correction factors of the target components, and the standard curves of the components were plotted based on the correction factors. The abscissa (*X*-axis) represents the peak area of the sample substance, while the ordinate (*Y*-axis) represents the concentration of the sample substance. The concentration of the sample substance was accurately calculated from the measured peak area according to the standard curve, and its exact content was further determined. The retention time of standard samples and the standard curves are provided in Table S1. The solid residue was washed thoroughly with deionized water and dried overnight in a vacuum oven at 105 °C. The product yield was calculated as the ratio of the weight of the detected product to the weight of cellulose initially charged into the reactor. Cellulose conversion was determined based on the weight difference of the dried solid residue before and after the reaction. Each experiment was performed in triplicate, and the absolute error in both product yield and cellulose conversion was controlled within 3%. Gas chromatography-mass spectrometry (GC-MS) was employed to analyze the organic compounds in the liquid product. The sample was dissolved in methanol following rotary evaporation, and detection was performed using an Agilent 9000 instrument. Detection method: the DB-624 chromatographic column was used; the initial temperature was 40 °C, the final temperature was 280 °C, and the heating rate was 10 °C min^{-1}. The analysis method for standard substances was the same as mentioned above.

3. Results and discussion

3.1 Analysis of the synthesized materials

Four imine-linked COFs were synthesized *via* a solvothermal method and subsequently employed as supports for the preparation of COF composites through a polyol reduction method. The synthesis route is illustrated in Fig. 1(a).

The XRD patterns of the four synthesized materials are shown in Fig. 1(b)–(e). TATP exhibits four distinct diffraction peaks at 5.65°, 9.77°, 14.64°, and 26.8°, corresponding to the (100), (200), (210), and (001) crystal planes, respectively. The (001) peak reflects the π–π stacking structure of the material, which is mainly attributed to hydrogen bonding interactions between adjacent layers. The sharp and well-defined diffraction peaks indicate a high degree of crystallinity, which is consistent with previous reports, further confirming the successful synthesis of the hydroxyl-functionalized COF.[27–29] Additionally, TBBT exhibits characteristic peaks at 2.4°, 7.6°, and 25.8°, while TBTP and TABT show peaks at $2\theta = 5.2°$, 16.8°, and 26.3°, corresponding to the (100), (110), and (002) planes, respectively, indicating the presence of highly ordered two-dimensional layered stacking structures. Simulated structural models of the four COFs generated using Material Studio are displayed in Fig. 1(f)–(i). Fig. 2(a) shows the XRD patterns of TATP after loading with Ru, WO_x, and Ru–WO_x. After loading Ru onto the

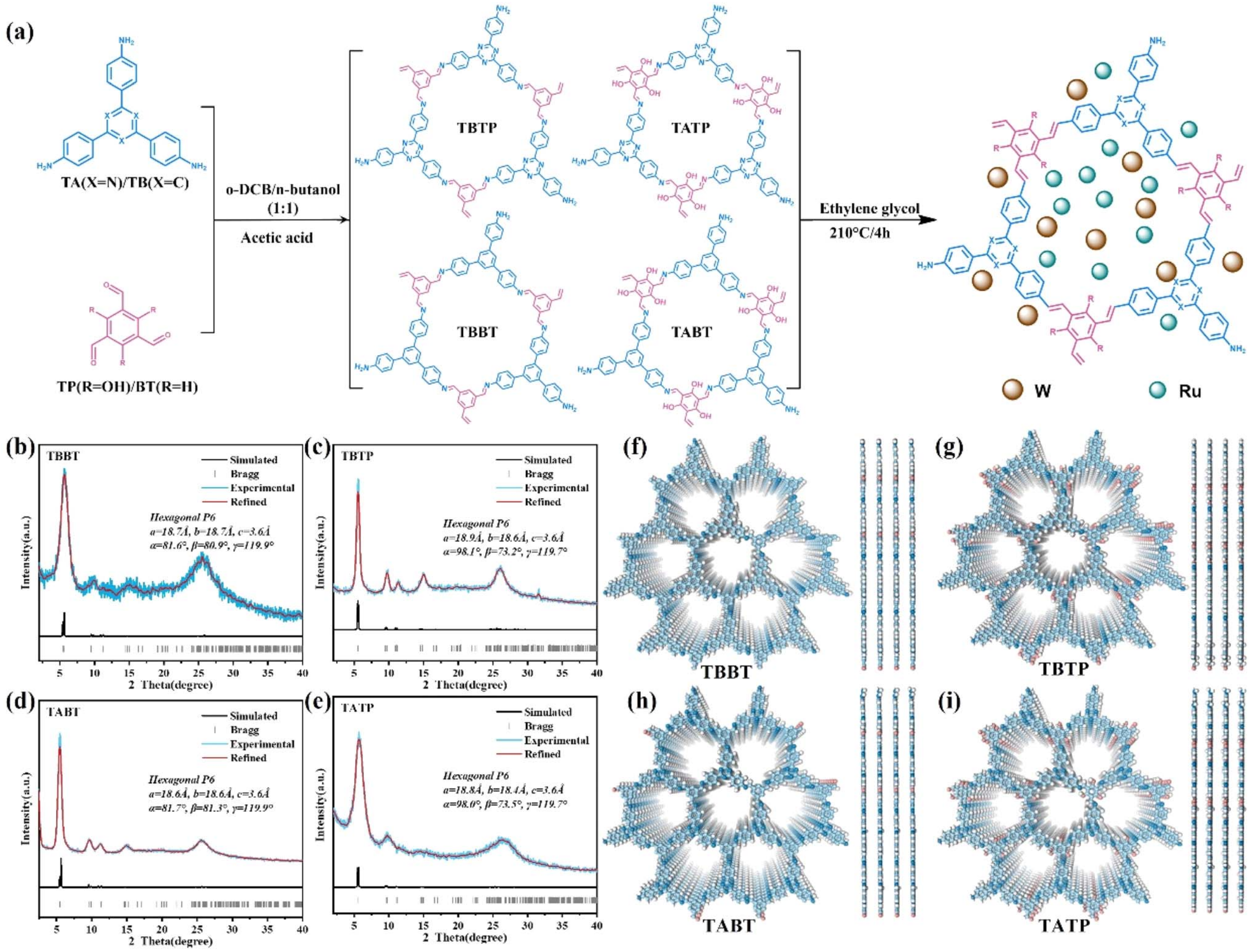

Fig. 1 (a) Schematic diagram of composite material synthesis; XRD patterns of TBBT (b), TBTP (c), TABT (d), and TATP (e); simulated structural models of TBBT (f), TBTP (g), TABT (h), and TATP (i).

TATP, the resulting composite retained the characteristic diffraction peaks of pristine TATP, although the overall peak intensities were reduced. No diffraction peaks corresponding to Ru metal were observed, suggesting that the crystal structure of TATP remained largely intact during the metal loading process and that the incorporation of Ru did not disrupt the framework. In contrast, when TATP was loaded with W, the resulting XRD pattern displayed strong crystalline peaks that matched well

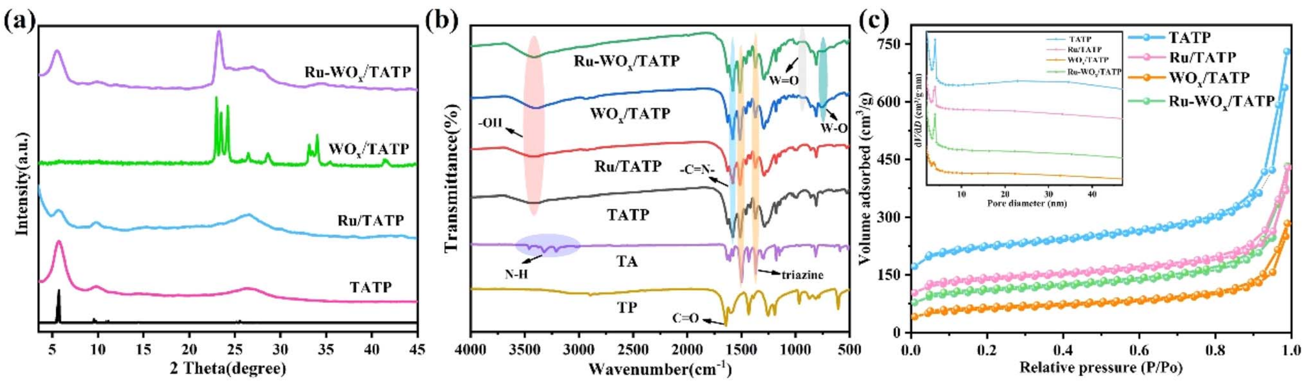

Fig. 2 (a) PXRD patterns; (b) FTIR spectra; (c) N_2 adsorption–desorption isotherms and corresponding pore size distributions of the synthesized materials.

with the monoclinic WO_3 phase (JCPDS: 43-1035), indicating the successful hydrolysis of WCl_6 into crystalline WO_3.[30] The diffraction peaks of TATP were no longer visible, likely due to the intense reflection signals from WO_3 overshadowing those of TATP. Upon co-loading with Ru and W, a sharp diffraction peak appeared around 23°, which matched well with monoclinic WO_x (JCPDS: 71-2450), confirming the successful incorporation of WO_x onto the TATP surface with the formation of a well-defined crystalline phase. Additionally, characteristic TATP peaks were still observed, indicating that its framework was preserved during the loading process. The co-loading and reduction process may have even contributed to the structural stability of the COF. The absence of detectable Ru diffraction peaks suggests that Ru nanoparticles are highly dispersed on the COF surface, likely in the form of ultrasmall nanoclusters. As shown in Fig. S1(a), the XRD patterns of Ru–WO_x-functionalized TBBT, TBTP, and TABT composites display generally weakened characteristic peaks compared to their pristine COF counterparts. This attenuation may result from the intercalation of Ru–WO_x species between COF layers, leading to expanded interlayer spacing and disruption of the original periodic structure, thereby reducing crystallinity. Moreover, no characteristic peaks of Ru metal were detected, further confirming the high dispersion of Ru nanoparticles in the composite materials.

The FTIR spectra of TATP and its metal-loaded derivatives are presented in Fig. 2(b). The broad absorption band in the 3000–3800 cm^{-1} range for TATP is attributed to adsorbed water and the O–H stretching vibration from the TP precursor.[27] The C=O stretching band around 1625 cm^{-1} is significantly weakened compared to that of TP.[31] The C=O peak near 1700 cm^{-1} in Fig. S1(b) is mainly derived from the aldehyde vacancy at the end of COF. In addition, the N–H stretching bands observed at 3208 cm^{-1}, 3322 cm^{-1}, and 3460 cm^{-1}, which are characteristic of amino groups, are nearly absent relative to those in TA. Meanwhile, the enhanced and broadened absorption bands at approximately 1610 cm^{-1} and 1581 cm^{-1} are assigned to the C=N stretching vibrations in the imine linkages, indicating the successful formation of imine bonds.[32,33] The FTIR spectrum of TATP also retains characteristic peaks at 3433 cm^{-1}, 1365 cm^{-1}, and 1496 cm^{-1}, corresponding to –O–H (from phenolic hydroxyl groups), C–N–C, and C–N vibrations within the triazine ring, further confirming the presence of both phenolic and triazine structural units in TATP. For WO_x/TATP and Ru–WO_x/TATP, additional bands appear at 751 cm^{-1} and 936 cm^{-1}, corresponding to the stretching vibrations of W=O and W–O bonds, respectively, demonstrating the successful incorporation of tungsten oxides onto the TATP surface.[34,35] Moreover, the FTIR spectra of Ru/TATP, WO_x/TATP, and Ru–WO_x/TATP closely resemble that of pristine TATP, indicating that the metal loading process does not significantly alter the chemical structure or connectivity of the TATP framework. Fig. S1(b) displays the FTIR spectra of TBBT, TABT, and TBTP before and after Ru–WO_x functionalization. Compared with the monomer precursors, the characteristic absorption bands of amino (–NH_2, ∼3300 cm^{-1}) and aldehyde (–CHO, ∼1680 cm^{-1}) groups are markedly reduced in intensity in the functionalized materials. This trend is consistent with that observed in TATP and suggests that the Schiff-base condensation reaction effectively consumed the active functional groups, confirming the formation of imine linkages. Notably, all three COFs exhibit strong absorption bands at 1595 cm^{-1}, corresponding to the stretching vibrations of C=N bonds, further validating the successful construction of the COFs. In addition, TBTP shows a broad absorption band in the range of 3095–3495 cm^{-1}, attributed to the O–H stretching vibrations of phenolic groups, while TABT exhibits a sharp peak at 1360 cm^{-1}, characteristic of C–N vibrations in the triazine ring. These specific vibrational signals provide spectroscopic evidence supporting the precise construction of structurally distinct COFs. After Ru–WO_x functionalization, the FTIR spectra of Ru–WO_x/TBBT, Ru–WO_x/TBTP, and Ru–WO_x/TABT composites retain the characteristic peaks of their respective COF supports, while also showing new absorption bands at 874 cm^{-1} and 682 cm^{-1}. These are assigned to the asymmetric stretching vibration of W=O and the symmetric stretching vibration of W–O–W, respectively. This confirms that WO_x species are successfully anchored onto the COF surfaces through chemical interactions without disrupting the main framework structure. Fig. 2(c) shows the nitrogen adsorption–desorption isotherms and pore size distributions of TATP, Ru/TATP, WO_x/TATP, and Ru–WO_x/TATP. All four materials exhibit typical type IV isotherms, indicating mesoporous structures, with average pore sizes of 5.4 nm, 3.6 nm, 5.2 nm, and 6.7 nm, respectively. Compared with TBBT (168.5 $m^2\ g^{-1}$), TBTP (331.6 $m^2\ g^{-1}$), and TABT (273.6 $m^2\ g^{-1}$) (Table S2), TATP has a larger specific surface area (831.9 $m^2\ g^{-1}$), demonstrating its potential as an efficient catalyst support. After loading with Ru or WO_x nanoparticles, the specific surface areas decrease to 510.2 $m^2\ g^{-1}$, 218.8 $m^2\ g^{-1}$, and 394.4 $m^2\ g^{-1}$ for Ru/TATP, WO_x/TATP, and Ru–WO_x/TATP, respectively, due to partial occupation of the COF nanochannels by the metal nanoparticles. Notably, the loading of Ru may facilitate the dispersion of WO_x, resulting in a smaller decrease in the specific surface area of Ru–WO_x/TATP compared with WO_x/TATP. Fig. S3 presents the TGA curves of TATP, Ru/TATP, WO_x/TATP, and Ru–WO_x/TATP. Two major weight loss events are observed around 230 °C and 490 °C. The former is attributed to the decomposition of trace solvent molecules adsorbed within the pores, while the latter corresponds to the rapid decomposition of the frameworks above ∼490 °C. Among the four materials, TATP exhibits a notably higher mass loss than the others. These results confirm that all four materials exhibit excellent thermal stability under catalytic conditions.

The chemical composition and oxidation states of the synthesized materials were investigated using XPS. As shown in Fig. S4(a), the survey spectra reveal that all four materials contain light elements such as C, O, and N, which are the main constituents of the TATP framework. In Fig. 3, Ru is detected in Ru/TATP, W in WO_x/TATP, and both Ru and W are present in the Ru–WO_x/TATP composite. Fig. 3(a) presents the high-resolution N 1s spectra of the four samples. All spectra display peaks at binding energies of 398.5 eV, 399.9 eV, and 400.5 eV, which can be assigned to C=N in imine bonds, C–N in triazine rings, and –NH functional groups, respectively, confirming the

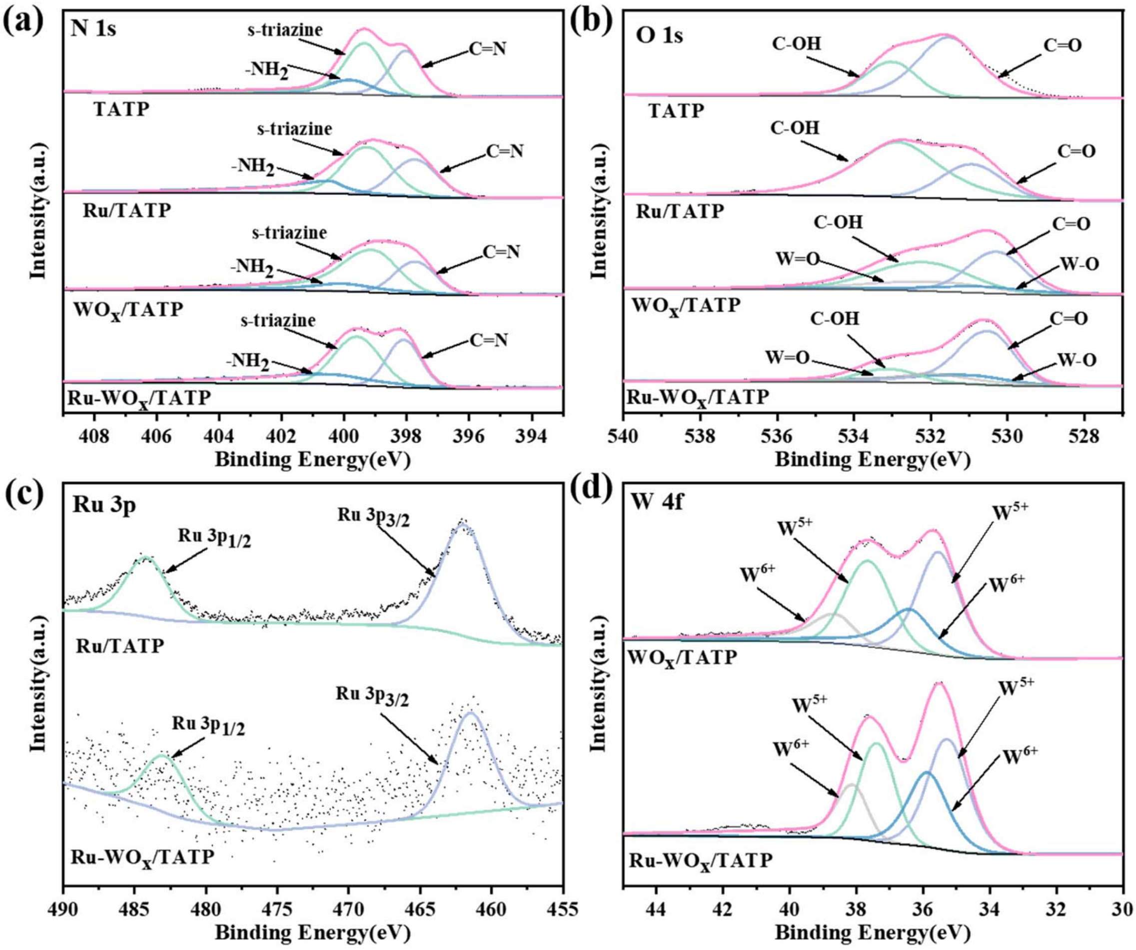

Fig. 3 XPS spectra of the synthesized materials: (a) N 1s spectrum; (b) O 1s spectrum; (c) Ru 3p spectrum; (d) W 4f spectrum.

successful formation of imine linkages.[32,36] The O 1s spectra in Fig. 3(b) show peaks at 531.6 eV and 533.1 eV, corresponding to C═O and C–O bonds, respectively, indicating the presence of unreacted aldehyde groups and phenolic hydroxyl groups in TATP.[37,38] Additionally, in WO_x/TATP and Ru–WO_x/TATP, peaks at 530.8 eV and 532.6 eV are observed, which are attributed to W–O and W═O bonds, respectively. As illustrated in Fig. 3(c), Ru/TATP and Ru–WO_x/TATP exhibit characteristic peaks of metallic Ru^0 at 461.9 eV and 484.2 eV, corresponding to Ru $3p_{1/2}$ and Ru $3p_{3/2}$ orbitals, indicating that Ru^{3+} was successfully reduced to its metallic state. Fig. 3(d) shows the high-resolution W 4f spectra of WO_x/TATP and Ru–WO_x/TATP. Peaks at 35.6 eV and 37.7 eV are assigned to W^{5+} $4f_{5/2}$ and $4f_{7/2}$, while peaks at 36.4 eV and 38.6 eV correspond to W^{6+} species. These results confirm that tungsten exists in an oxidized state on the COF surface. The presence of W^{6+} is likely due to partial hydrolysis of WCl_6 forming WO_3, while the W^{5+} species indicate partial reduction during the synthesis.[39,40] In the XPS spectra, the W 4f binding energies in WO_3 (36.4 eV and 38.6 eV) exhibit a slight positive shift compared to pure WO_3 (35.8 eV) (Fig. 3(d)), indicating a decrease in electron density around W atoms. This shift likely arises from interactions between WO_3 and the N atoms (terminal amino groups and imine bonds) in the COFs, thereby enhancing binding stability.[41,42] Moreover, in the FTIR spectra, the stretching vibration of COF amino groups shifts from 3280 cm^{-1} to 3240 cm^{-1} upon WO_3 loading, suggesting the formation of hydrogen bonds that further reinforce the interaction between COFs and WO_3.[43] The XPS survey spectra of Ru–WO_x-loaded TBBT, TBTP, and TABT are presented in Fig. S4(b). As shown in the deconvoluted N 1s spectra (Fig. S5(a)), all three materials exhibit peaks at binding energies of 397.9 eV and 401.3 eV, corresponding to nitrogen atoms in imine (C═N) and amine (–NH_2) groups. Notably, Ru–WO_x/TABT also shows an additional peak at 399.1 eV, which can be attributed to pyrazine nitrogen within the triazine ring. These findings further confirm the successful Schiff-base condensation and the incorporation of triazine structures, consistent with FTIR results. Fig. S5(b) presents the deconvoluted O 1s spectra. All samples exhibit a characteristic peak near 531.0 eV corresponding to C═O groups. In addition, Ru–WO_x/TBTP and Ru–WO_x/TABT show a peak at 530.0 eV, which is attributed to phenolic –OH groups. This indicates that the phenolic hydroxyl groups remain intact on the surfaces of TBTP and TABT. In contrast, the absence of this peak in Ru–WO_x/TBBT suggests structural differences, which aligns with the FTIR observations. Fig. S5(c) and (d) show the high-resolution Ru 3p and W 4f spectra, respectively. The Ru 3p spectra display peaks at 461.1 eV and 483.7 eV, corresponding to Ru $3p_{3/2}$ and $3p_{1/2}$ of metallic Ru^0, consistent with the standard binding energies of elemental Ru. The deconvoluted W 4f spectra show two pairs of peaks: 34.4 eV and 36.6 eV correspond to W^{5+} $4f_{7/2}$ and $4f_{5/2}$, while 35.1 eV and 37.4 eV are assigned to W^{6+} species. These results confirm that WO_x is primarily present in mixed oxidation states, with W^{5+} as the dominant species. The presence of W^{6+} is likely due to the formation of oxygen vacancies during the reduction process.[44]

The SEM images of TATP are shown in Fig. 4(a) and (b). The material exhibits a fibrous morphology with lengths ranging from 0.5 to 1 μm and an average width of approximately 100 nm. As observed in the TEM images in Fig. 5(a) and (b), the fibrous structure of TATP is composed of interwoven nanosheets. Fig. 4(c) and (d) shows that Ru nanoparticles are uniformly dispersed on the surface of TATP. The partial coverage of TATP crystals by Ru nanoparticles may disrupt the ordered packing of the framework, leading to a reduction in the intensity of the XRD peaks. As shown in Fig. 4(c)–(h), the Ru/TATP, WO_x/TATP, and Ru–WO_x/TATP composites retain the fibrous morphology, forming an interwoven porous network. The introduction of Ru and W metals does not significantly alter the microstructure of the TATP framework. The TEM images in Fig. 5(g) and (h) reveal that numerous nanoparticles and nanorods are homogeneously distributed on the surface of the TATP nanosheets. Lattice fringes with an interplanar spacing of 0.21 nm correspond to the (101) plane of metallic Ru nanoparticles,[45] while a spacing of 0.24 nm is assigned to the (110) plane of WO_x nanorods,[46] confirming the successful deposition of both Ru and W on the TATP nanosheet surface. Fig. 4(i)–(l) show the EDX elemental mapping images of Ru–WO_x/TATP, indicating the uniform distribution of C, N, O, Ru, and W elements across the catalyst surface. These results further verify the successful incorporation of Ru and W into the Ru–WO_x/TATP composite, which is consistent with the XRD analysis. Fig. S6 presents the SEM images of three comparison COFs before and after metal loading. TBBT exhibits a typical layered nanosheet structure with lateral dimensions of approximately 200–300 nm. After functionalization, the nanosheets show significant fragmentation, and the lateral size decreases to 100–150 nm, which may be attributed to structural stress caused by chemical modification during the loading process. TBTP and TABT exhibit interpenetrated porous fibrous network structures before functionalization. The average fiber width of TBTP is approximately 100 ± 15 nm, while that of TABT is about 150 ± 20 nm. The difference in morphology may result from variations in polymerization kinetics induced by the steric effects of different monomers. After functionalization, the fibrous framework of both materials remains intact. However, higher magnification images reveal the presence of uniformly distributed nanoparticles (5–10 nm) on the fiber surfaces. EDX elemental mapping (Fig. S7) confirms that these nanoparticles are Ru–WO_x clusters, indicating the successful anchoring of bimetallic species onto the COF surfaces.

3.2 Catalytic conversion of cellulose to EG

A series of synthesized catalysts were applied in the one-pot aqueous-phase catalytic conversion of cellulose to EG under reaction conditions of 245 °C, 180 min, and 5 MPa H_2. The catalytic results are summarized in Table 1. In the blank control experiment without any catalyst, the cellulose conversion

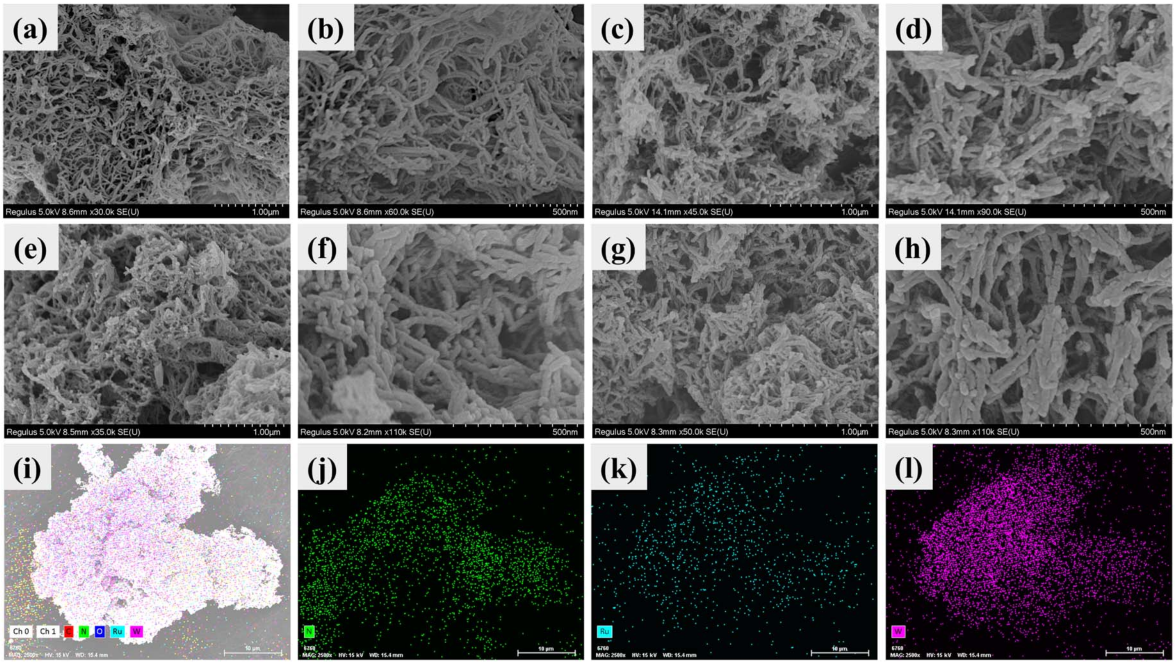

Fig. 4 SEM images of the synthesized materials: (a and b) TATP; (c and d) Ru/TATP; (e and f) WO_x/TATP; (g and h) Ru–WO_x/TATP; (i–l) EDX elemental mapping images of Ru–WO_x/TATP.

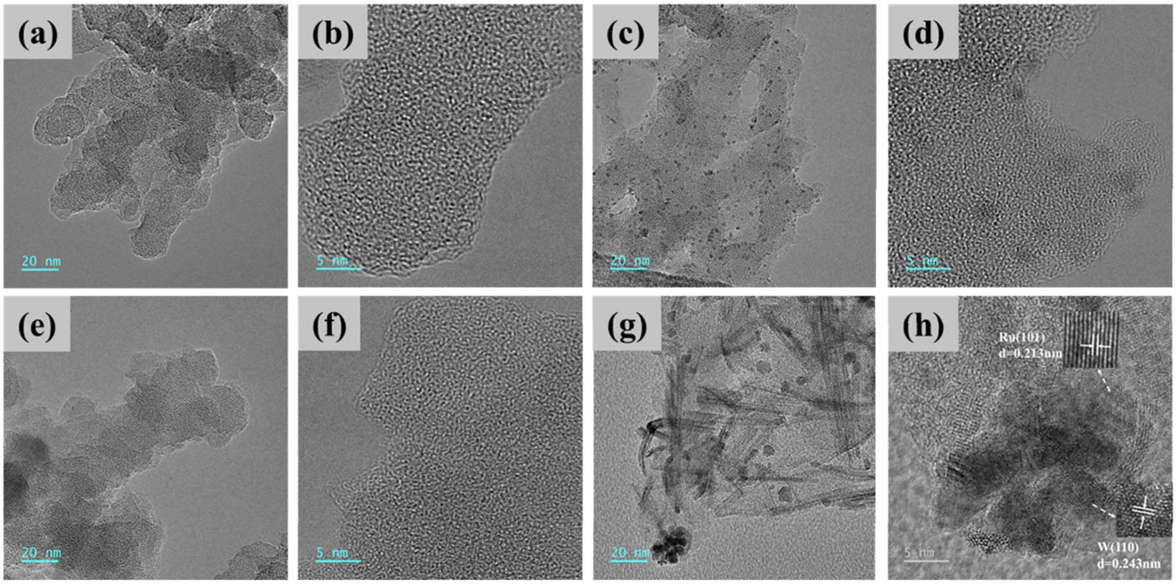

Fig. 5 TEM images of the synthesized materials: (a and b) TATP; (c and d) Ru/TATP; (e and f) WO_x/TATP; (g and h) Ru–WO_x/TATP.

reached 78.5%, but only a trace amount of EG (1.1%) was detected in the product. This indicates that although H^+ in liquid water at high temperature can promote cellulose hydrolysis, most of the cellulose was converted into oligosaccharides or humins rather than EG.[47,48] When COF material TATP, containing bifunctional groups (phenolic hydroxyl and triazine ring), was used as the catalyst, the cellulose conversion increased to 86.8%, but the EG yield remained low (1.7%). This is likely due to the partial proton donation by the phenolic hydroxyl groups in TATP, which facilitated the cleavage of β-1,4-glycosidic bonds in cellulose, forming glucose and oligosaccharides.[49] Upon using Ru/TATP, a COF loaded with Ru metal, the cellulose conversion reached 93.1%, and the EG yield significantly increased to 30.3%, demonstrating that Ru plays a key role in promoting the hydrogenation step and enhancing EG formation. The use of WO_x/TATP resulted in a slightly improved EG yield compared to pure TATP (8.69%), but the yield remained relatively low, possibly due to the absence of hydrogenation-active sites in WO_x/TATP, which are critical for the hydrogenation step in EG production. To address this, a bifunctional catalyst Ru–WO_x/TATP was synthesized by co-loading Ru and W onto TATP. This catalyst achieved complete cellulose conversion with an EG yield of 62.9%. Compared with Ru–WO_x/TATP, the EG yields of Ru–WO_x/TBTP and Ru–WO_x/TABT under identical conditions were slightly lower, at 60.4% and 60.1%, respectively, confirming the synergistic catalytic effect between the two functional groups. Notably, Ru–WO_x/TBBT, which lacks acidic functional groups, exhibited significantly lower catalytic performance, with an EG yield of only 45.1%, further verifying the essential role of acidic sites in the hydrolysis of cellulose. The performance difference among catalysts suggests that the synergy between phenolic hydroxyl and triazine functionalities enhances catalytic efficiency through the following mechanisms: (1) phenolic hydroxyl groups act as Brønsted acid sites to facilitate the cleavage of glycosidic bonds in cellulose; (2) triazine rings serve as Lewis base sites, stabilizing reaction intermediates and suppressing side reactions; (3) the bimetallic Ru–WO_x species provide multiple active sites and modulate the reaction pathway *via* electronic effects. These findings align well with previously reported concepts in multifunctional catalyst design. Based on the above results, Ru–WO_x/TATP, which exhibited the best catalytic performance, was selected as the model catalyst for subsequent optimization studies, aiming to further elucidate the reaction mechanism and establish a structure–activity relationship model.[50,51]

Table 1 One-pot catalytic conversion of cellulose to EG using synthesized COFs as catalysts[a]

Entry	Sample	Conversion	Yield of EG	Selectivity
1	No catalyst	78.5%	1.1%	1.1%
2	TATP	86.8%	1.7%	2.0%
3	Ru/TATP	93.1%	30.3%	32.5%
4	WO_x/TATP	92.6%	8.7%	9.4%
5	Ru–WO_x/TBBT	100%	45.1%	45.1%
6	Ru–WO_x/TBTP	100%	60.4%	60.4%
7	Ru–WO_x/TABT	100%	60.1%	60.1%
8	Ru–WO_x/TATP	100%	62.9%	62.9%

[a] Reaction conditions: 245 °C for 180 min under 5 MPa H_2 in 50 mL H_2O with 0.5 g cellulose and 0.15 g catalyst.

Using Ru–WO_x/TATP as the catalyst, the effects of various parameters, including metal loading, catalyst dosage, reaction temperature, and reaction time, on the aqueous-phase catalytic conversion of cellulose to EG were systematically investigated. The influence of metal loading on catalytic performance is shown in Fig. 6. As illustrated in Fig. 6(a), under the reaction conditions of 245 °C, 180 min, and 5 MPa H_2, complete conversion of cellulose was achieved. With increasing Ru loading, the cellulose conversion remained unaffected, while the EG yield exhibited a volcano-type trend. The maximum EG yield was observed at a Ru loading of 3 wt%. Further increases in Ru content led to a decline in EG yield, which is likely attributed to the excessive hydrogenation activity introduced by the high Ru content. This promoted the formation of byproducts such as 1,2-butanediol and 1,6-hexanediol, thereby reducing the EG selectivity.[52,53] The effect of W loading on catalytic performance is presented in Fig. 6(b). When the W content was below 25 wt%, the cellulose conversion remained at 100%, but the EG yield was lower than 50%, accompanied by a higher yield of byproducts. This may be due to insufficient support for redox processes during the reaction, resulting from the inadequate W loading. As the W content increased to 30 wt%, the catalyst exhibited optimal performance, with the highest EG yield of 62.9% and the lowest yields of byproducts (1,2-butanediol and 1,6-hexanediol at 5.5% and 4.52%, respectively). However, further increasing the W content led to a gradual decline in EG yield and an increase in byproduct formation, which is unfavorable for selective EG production. These results demonstrate that the loadings of Ru and W play a crucial role in determining the catalytic performance. Excessive metal content may lead to the overproduction of undesired byproducts, ultimately compromising the selectivity toward EG.

Catalyst dosage is another crucial factor affecting catalytic performance. Therefore, we systematically evaluated the effect of catalyst amount on the conversion of cellulose to EG, and the results are presented in Fig. 7. As shown in Fig. 7(a), the EG yield initially increased and then decreased with increasing catalyst dosage. The maximum EG yield of 62.9% was achieved at a catalyst loading of 150 mg. Further increase in catalyst amount negatively impacted the reaction equilibrium and product yield, thereby hindering further improvement in EG production. Fig. 7(b) illustrates the influence of reaction temperature on catalytic performance. As the temperature increased from 215 °C to 255 °C, the EG yield exhibited a volcano-shaped trend, while cellulose conversion continuously increased. Complete conversion of cellulose was observed at 235 °C. Elevated temperatures facilitated the cleavage of β-1,4-glycosidic bonds in cellulose and promoted selective C–C bond cleavage of glucose, which is favorable for the subsequent hydrogenation of glycolaldehyde to EG.[54] However, excessively high temperatures were detrimental to EG formation. The decrease in EG yield at higher temperatures may be attributed to the occurrence of side reactions and thermal degradation of the product, resulting in reduced selectivity.[55]

The effect of reaction time on EG yield is shown in Fig. 7(c). As the reaction time increased from 60 min to 180 min, the EG yield rose sharply from 29.74% to a maximum of 62.9%. However, a further extension of reaction time led to a gradual decline in EG yield. This could be due to the overexposure of EG to prolonged reaction conditions, causing further degradation of the product.[56]

Given that the catalytic reaction is carried out under high-temperature and high-pressure conditions, catalyst stability is critically important for practical applications. The reusability of the Ru–WO_x/TATP catalyst was evaluated, and the results are shown in Fig. 8. As illustrated in Fig. 8(a), after three consecutive reaction cycles, cellulose conversion remained at 100%, while the EG yield decreased from 62.9% to 42.6%, indicating a decline in catalytic selectivity during reuse. To address this issue, a combined catalytic system of Ru/TATP and WO_3 was tested for cellulose conversion, as shown in Fig. 8(b). After five successive cycles, cellulose was still fully converted, and the EG yield only slightly decreased from 60.7% to 53.2%, demonstrating superior stability and reusability of the Ru/TATP + WO_3 system. The decline in the catalytic performance of Ru–WO_x/TATP may be attributed to the transformation of WO_x into water-soluble tungsten bronzes during the reaction. This hypothesis is further supported by the observation that the post-reaction solution exhibited a blue color, characteristic of tungsten bronze formation.[49] Fig. S8 presents the XRD patterns of the Ru–WO_x/TATP catalyst before and after use. The characteristic diffraction peaks remain unchanged after three catalytic cycles, indicating that the catalyst retains its structural integrity and crystallinity during the reaction.

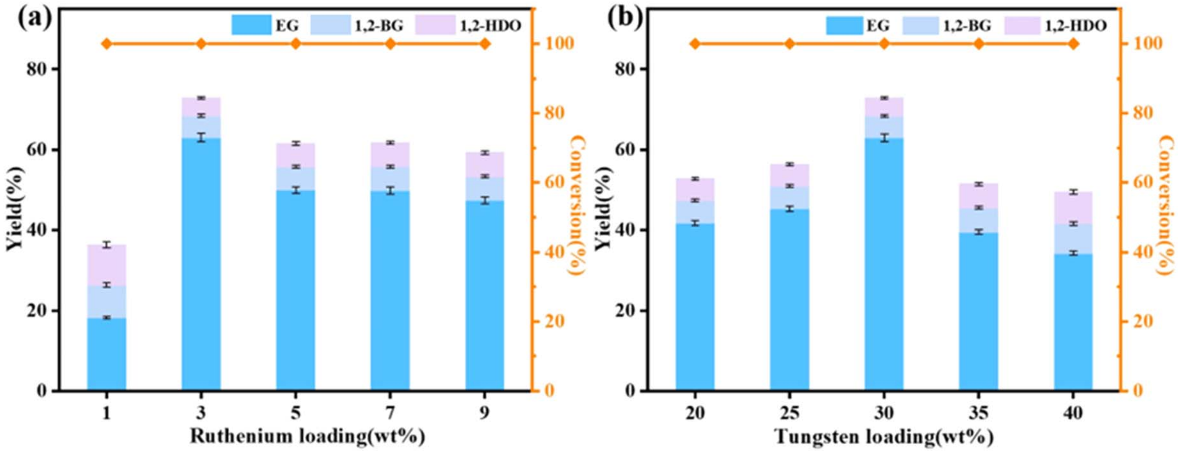

Fig. 6 Effect of (a) Ru and (b) W loading on the aqueous-phase catalytic conversion of cellulose to EG.

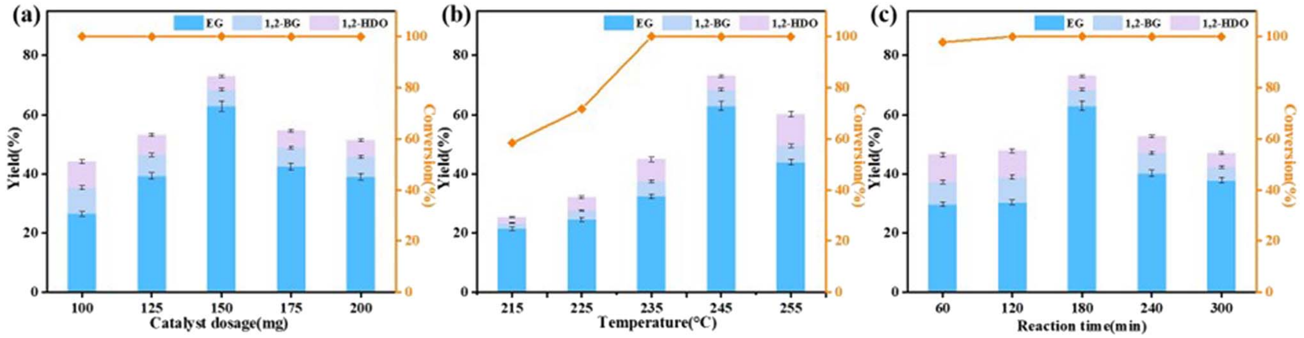

Fig. 7 Effects of (a) catalyst dosage, (b) reaction temperature, and (c) reaction time on catalytic performance.

The elemental distribution of the catalyst before and after use was analyzed *via* scanning electron microscopy coupled with energy dispersive X-ray spectroscopy (SEM-EDX) to conduct semi-quantitative calculations of the Ru and WO_3 loadings. After catalytic application, the Ru content decreased slightly from 0.36 to 0.22 at%, while the W content decreased from 1.12 to 0.95 at%. This moderate reduction is attributed to the partial detachment of metal nanoparticles during the catalytic process. Consistent with these observations, the catalytic activity exhibited a gradual decline upon repeated recycling, further confirming that nanoparticle detachment adversely affects catalytic performance.

Control experiments were conducted using Ru nanoparticles (NPs), WO_x NPs, and Ru–WO_x (without a COF support) as catalysts, with the results summarized in Table S6. Ru NPs achieved a cellulose conversion of 82.4% but a low EG yield of 7.05%, indicating that hydrogenation activity alone is insufficient to drive cellulose hydrolysis and C–C bond cleavage.[57] WO_x NPs gave a conversion of 86.6% and an EG yield of 9.83%, suggesting that acid sites alone cannot complete the subsequent hydrogenation, with the products mainly consisting of unhydrogenated small-molecule aldehydes (*e.g.*, glycolaldehyde). The physical mixture of Ru–WO_x improved the conversion to 95.3% and the EG yield to 31.17%, demonstrating basic synergy between Ru and WO_x. However, these values remain significantly lower than those of Ru–WO_x/TATP (cellulose conversion: 100%; EG yield: 62.9%), confirming that the COF support functions not merely as a physical scaffold but also contributes to synergistic catalysis.

Table 2 summarizes representative studies on the catalytic conversion of cellulose to EG, comparing their reaction conditions and EG yields with those achieved in this work. Under identical conditions, the catalysts developed here, Ru–WO_x/TATP, Ru–WO_x/TBTP, and Ru–WO_x/TABT, achieved EG yields of 62.9%, 60.4%, and 60.1%, respectively, significantly outperforming reference systems such as Pd@W/Al–$MSiO_2$ (56.5%), Co/CeO_x (53.7%). Notably, the cellulose-to-catalyst ratio in this study reached 10 : 3, considerably lower than those in other systems (*e.g.*, cellulose : Ni–WO_x/SAPO-11 = 2 : 1, cellulose : Ru–WO_x/SiO_2 (500 Å) = 1 : 1), underscoring the reduced catalyst loading required by the present system. Moreover, Ru–WO_x/TATP enabled complete cellulose conversion (100%) under relatively mild conditions, namely 5 MPa H_2 and a 3 h reaction time, whereas other solid acid catalysts required harsher conditions, such as 6 MPa H_2 for 6 h (Co/CeO_x) or 4 MPa H_2 for 5 h (Ru–WO_x/SiO_2 (500 Å)). This highlights the system's lower energy and equipment pressure demands. In summary, Ru–WO_x/TATP combines high EG yield with milder

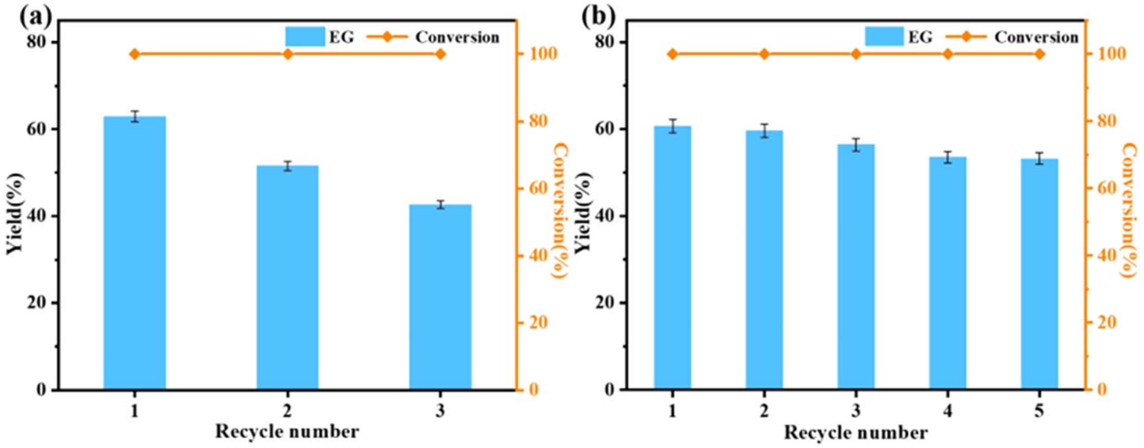

Fig. 8 Recycling performance of (a) Ru–WO_x/TATP and (b) Ru/TATP + WO_3 catalysts in the catalytic conversion of cellulose.

Table 2 Comparison of functionalized COFs and other multifunctional catalysts in the catalytic conversion of cellulose to EG

Entry	Catalyst	Reaction conditions	Catalyst dosage (cellulose : catalyst)	Yield of EG	Ref.
1	Ni–WO_x/SAPO-11	240 °C, 4 MPa H_2, 4 h	2 : 1	66.6%	58
2	Co/CeO_x	245 °C, 6 MPa H_2, 6 h	6 : 5	53.7%	59
3	Pd/o-WO_3	245 °C, 5.5 MPa H_2, 4 h	2 : 1	64.8%	40
4	Pd/o-WO_3	245 °C, 5.5 MPa H_2, 4 h	4 : 1	61.2%	
5	Pd@W/Al–$MSiO_2$	240 °C, 4 MPa H_2, 2 h	5 : 3	56.5%	60
6	NiCu/WO_3	245 °C, 5.5 MPa H_2, 4 h	3 : 2	58.9%	57
7	Ru–WO_x/SiO_2 (500 Å)	240 °C, 4 MPa H_2, 5 h	1 : 1	51.5%	61
8	Ru–WO_x/TBBT	245 °C, 5 MPa H_2, 3 h	10 : 3	45.1%	This work
9	Ru–WO_x/TBTP	245 °C, 5 MPa H_2, 3 h	10 : 3	60.4%	This work
10	Ru–WO_x/TABT	245 °C, 5 MPa H_2, 3 h	10 : 3	60.1%	This work
11	Ru–WO_x/TATP	245 °C, 5 MPa H_2, 3 h	10 : 3	62.9%	This work

operating conditions, offering distinct advantages over conventional catalytic systems and presenting a more efficient and sustainable route for cellulose valorization.

3.3 Possible catalytic reaction mechanism

As illustrated in Fig. 9, a possible reaction mechanism for the Ru–WO_x/TATP-catalyzed conversion of cellulose to EG is proposed. The TATP framework possesses a highly porous structure with a large specific surface area, which facilitates the exposure of more active sites and provides sufficient space for cellulose degradation. In the initial stage of the reaction, the combined Brønsted acidity from hot water, phenolic –OH groups in the COF framework, and protons released from H_xWO_3 promotes the protonation of cellulose.[62,63] This activation weakens the 1,4-β-glycosidic bonds and hydrogen bonds, accelerating cellulose dissolution and hydrolysis into glucose and oligosaccharides.

Meanwhile, W^{5+} species on the catalyst surface create abundant oxygen vacancies, which adsorb oxygen atoms from the glycosidic linkages and α-OH groups.[54,64] Concurrently, oxygen-containing groups in WO_x interact with protons to form W–OH intermediates.[65] Glucose and oligosaccharides then undergo retro-aldol condensation catalyzed by H_xWO_3, resulting in cleavage of C–C and C–O bonds and formation of erythrose and an enediol intermediate. The latter undergoes further rearrangement to yield glycolaldehyde, which is subsequently hydrogenated over Ru active sites to produce EG.[11,66] However, various side reactions may occur in parallel. For instance, glucose can isomerize to fructose, which may then be hydrogenated to C_6 sugar alcohols or dehydrated to lactic acid. Retro-aldol cleavage of erythrose and fructose may also yield byproducts such as 1,2-butanediol, 3-hydroxytetrahydrofuran, and 1,2-propanediol, all of which compete with the desired EG formation pathway and lower product selectivity. In summary, the catalytic hydrogenolysis of cellulose to EG involves a complex reaction network centered on glucose retro-aldol fragmentation, accompanied by multiple competing pathways. High EG selectivity hinges on the fine-tuning of intermediate reaction rates. The Ru–WO_x/TATP

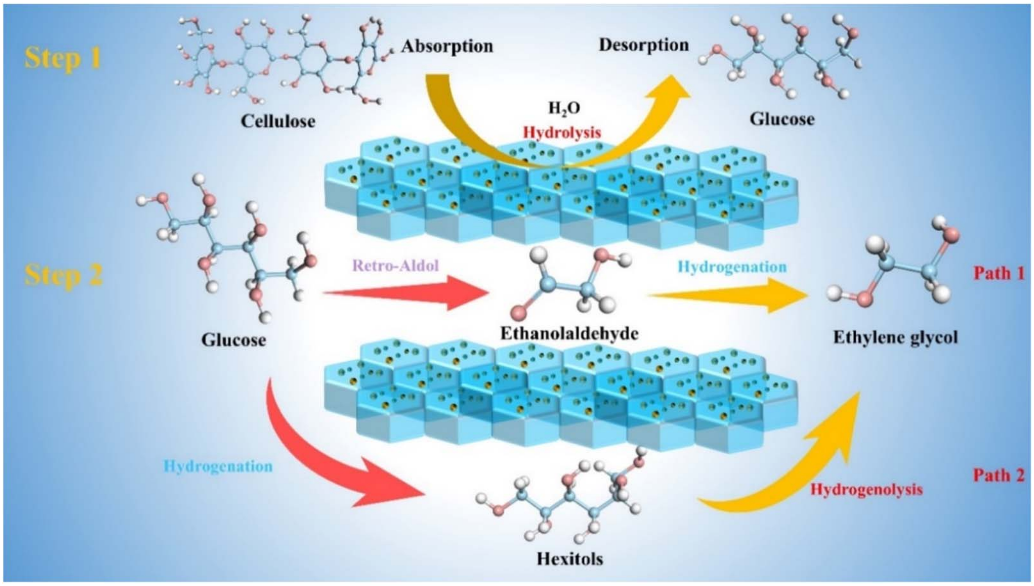

Fig. 9 Proposed reaction mechanism of cellulose conversion to EG catalyzed by Ru–WO_x/TATP.

catalyst synergistically combines optimized Brønsted acidity, oxygen vacancy density (*via* W^{5+}/W^{6+}), and Ru-mediated hydrogenation activity, thereby achieving complete cellulose conversion and a high EG yield of 62.9%.

Fig. S11 and Table S4 show the gas chromatography-mass spectrometry (GC-MS) spectrum and product information of the liquid products after the catalytic reaction. Through analysis, the possible composition of substances in the liquid products was clarified, which further provides a basis for improving the possible pathway of the catalytic reaction. As can be seen from Fig. S11 and Tables S1 and S4, in addition to the target product EG, major substances also include ethanol, levulinic acid, butanediol, hexanediol, and glycerol were also detected in the liquid products of the reaction. The presence of these products can reflect the conversion law of the reaction to a certain extent: cellulose first undergoes hydrolysis to generate glucose (or oligosaccharides), and the detection of 5-hydroxymethylfurfural (5-HMF) suggests that glucose may undergo a dehydration side reaction; the presence of levulinic acid may be derived from the further hydrolysis of 5-HMF, indicating that some dehydrated products do not convert according to the target pathway but undergo a subsequent ring-opening hydrolysis process. In addition, as the target product, the formation of ethylene glycol should correspond to the selective cleavage of the carbon chain in glucose units and the hydrogenation process; the appearance of polyols such as glycerol, 1,2-butanediol, 1,4-butanediol, and 1,2-hexanediol may be due to the different degrees of cleavage of intermediate products generated after cellulose hydrolysis during the catalytic process, leading to the formation of polyol by-products; small-molecule alcohols such as ethanol may be derived from the deep hydrogenation reduction of short-carbon-chain intermediates. The sorting of the above product information lays a foundation for the subsequent speculation of the specific steps and reaction mechanism of the catalytic reaction.

4. Conclusions

In this study, an imine-based COF rich in hydroxyl functional groups was synthesized *via* a solvothermal method. By incorporating active metals Ru and W, a functionalized COF catalyst, Ru–WO_x/TATP, exhibiting catalytic activities for hydrolysis, hydrogenolysis, and hydrogenation was successfully developed. This catalyst was applied to the one-step catalytic conversion of cellulose to ethylene glycol, demonstrating excellent performance. Under reaction conditions of 245 °C and 5 MPa H_2, cellulose conversion reached 100%, with an ethylene glycol selectivity of 62.9%. The superior catalytic activity of Ru–WO_x/TATP is attributed to proton generation from phenolic hydroxyl groups and the synergistic interaction between Ru and W active sites. These findings suggest a promising approach for utilizing COF materials in biomass catalytic conversion.

Author contributions

Yu Zhao and Yuan Ju: writing – original draft, visualization, methodology, investigation, formal analysis, data curation. Baozhen Guo: visualization, investigation. Peng Gan: visualization, investigation. Pengfei Lv: visualization, investigation. Jingli Yang: visualization, investigation. Chengcheng Qiao: visualization, investigation. Kai Zhang: writing – review & editing, supervision, project administration, methodology, funding acquisition.

Conflicts of interest

The authors declare no conflict of interest.

Data availability

All relevant information is provided in the SI. Further information and/or clarification can be provided by the authors upon request.

Supplementary materials include the relevant performance characterization of the synthesis and application processes of the COFs materials mentioned in the main text, as well as the quantitative and qualitative analysis results of the post-products. This is to help readers understand the content of the article more clearly and in-depth. See DOI: **https://doi.org/10.1039/d5ra05136c**.

Acknowledgements

This work was financially supported by the National Natural Science Foundation of China (Grant No. 22578235, 32101464), Shandong Provincial Key Research and Development Program (2024CXGC010412), Major Scientific Research Project for the Construction of State Key Lab (Grant No. 2025ZDGZ02), State Key Laboratory of Biobased Material and Green Papermaking (GZKF202121), and Taishan Scholar Foundation of Shandong Province.

References

1 Y. He, Y. Luo, M. Yang, Y. Zhang, M. Fan and Q. Li, *Catal. Sci. Technol.*, 2022, **12**, 4524–4534.
2 M. V. Rodionova, A. M. Bozieva, S. K. Zharmukhamedov, Y. K. Leong, J. Chi-Wei Lan, A. Veziroglu, T. N. Veziroglu, T. Tomo, J.-S. Chang and S. I. Allakhverdiev, *Int. J. Hydrogen Energy*, 2022, **47**, 1481–1498.
3 A. M. Raspolli Galletti, *Catalysts*, 2018, **8**, 398.
4 C. Wang, X. Zhang, Q. Liu, Q. Zhang, L. Chen and L. Ma, *Fuel Process. Technol.*, 2020, **208**, 106485.
5 A. Yadav, V. Sharma, M.-L. Tsai, C.-W. Chen, P.-P. Sun, P. Nargotra, J.-X. Wang and C.-D. Dong, *Bioresour. Technol.*, 2023, **381**, 129145.
6 Q. Zhang, E. Zhu, T. Li, L. Zhang and Z. Wang, *Biomacromolecules*, 2024, **25**, 6296–6318.
7 L. Wang, G. Li, X. Chen, Y. Yang, R. K. Liew, H. M. Abo-Dief, S. S. Lam, R. Sellami, W. Peng and H. Li, *Adv. Compos. Hybrid Mater.*, 2024, **7**, 219.
8 A. Wang, D. Austin, P. He, X. Mao, H. Zeng and H. Song, *Catal. Sci. Technol.*, 2018, **8**, 5632–5645.

9 X. Lei, G. Gu, Y. Hu, H. Wang, Z. Zhang and S. Wang, *Catalysts*, 2021, **11**, 736.

10 S. Kandasamy, S. P. Samudrala and S. Bhattacharya, *Catal. Sci. Technol.*, 2019, **9**, 567–577.

11 N. Enjamuri and S. Darbha, *Catal. Rev.*, 2024, **66**, 1137–1207.

12 M. K. Wong, S. S. M. Lock, Y. H. Chan, S. J. Yeoh and I. S. Tan, *Chem. Eng. J.*, 2023, **468**, 143699.

13 J. Ma, S. Shi, X. Jia, F. Xia, H. Ma, J. Gao and J. Xu, *J. Energy Chem.*, 2019, **36**, 74–86.

14 Y. Liu, W. Zhang and H. Liu, *Chin. J. Catal.*, 2023, **46**, 56–63.

15 Q. Yang, Y. Fan, J. Zhou and L. Zhao, *J. Cleaner Prod.*, 2023, **396**, 136540.

16 K. Ravi, H. Kachgunde, V. D. B. C. Dasireddy, J. Mensah, A. F. Lee, A. V. Biradar and K. Wilson, *Catal. Sci. Technol.*, 2025, **15**, 3149–3156.

17 N. Ji, T. Zhang, M. Zheng, A. Wang, H. Wang, X. Wang, Y. Shu, A. L. Stottlemyer and J. G. Chen, *Catal. Today*, 2009, **147**, 77–85.

18 K. Zhang, G. Yang, G. Lyu, Z. Jia, L. A. Lucia and J. Chen, *ACS Sustain. Chem. Eng.*, 2019, **7**, 11110–11117.

19 Z. Xiao, Q. Ge, C. Xing, C. Jiang, S. Fang, J. Ji and J. Mao, *J. Energy Chem.*, 2016, **25**, 434–444.

20 L. S. Ribeiro, A. L. F. Pires, J. J. d. M. Órfão and M. F. R. Pereira, *Renewable Energy*, 2022, **200**, 1008–1022.

21 M. S. Lohse and T. Bein, *Adv. Funct. Mater.*, 2018, **28**, 1870229.

22 A. López-Magano, A. Jiménez-Almarza, J. Alemán and R. Mas-Ballesté, *Catalysts*, 2020, **10**, 720.

23 H. Hu, Q. Yan, R. Ge and Y. Gao, *Chin. J. Catal.*, 2018, **39**, 1167–1179.

24 Z. Alsudairy, N. Brown, A. Campbell, A. Ambus, B. Brown, K. Smith-Petty and X. Li, *Mater. Chem. Front.*, 2023, **7**, 3298–3331.

25 J. Artz and R. Palkovits, *ChemSusChem*, 2015, **8**, 3832–3838.

26 P. Gan, K. Zhang, Z. Li, C. Zhang, G. Yang, L. Zhang, B. Wang and J. Chen, *Green Chem.*, 2024, **26**, 5155–5159.

27 X. Lin, Y. Deng, Y. He, J. Chen and S. Hu, *Appl. Surf. Sci.*, 2021, **545**, 149047.

28 S. Luo, T. Shu, M. Mao, H. Yu, Y. Zheng, D. Ding, L. Liu, K. Yao and J. Wang, *J. Energy Chem.*, 2024, **92**, 311–321.

29 M. Yu, Y. Chen, M. Gao, G. Huang, Q. Chen and J. Bi, *Small*, 2023, **19**, 2206407.

30 C. M. Kgoetlana, S. P. Malinga and L. N. Dlamini, *Catalysts*, 2020, **10**, 699.

31 X. Miao, F. Zhang, Y. Wang, X. Dong and X. Lang, *Sustainable Energy Fuels*, 2023, **7**, 1963–1973.

32 X. Lin, Y. He, Y. Zhang, W. Yu and T. Lian, *J. Membr. Sci.*, 2021, **638**, 119725.

33 Y. Zhang, Z. Chen, Z. Shi, T.-t. Lu, D. Chen, Q. Wang and Z. Zhan, *Sep. Purif. Technol.*, 2021, **275**, 119216.

34 Q. Wu, Z. Wang, B. Zhao, R. Zhao, S. Yu and L. Huang, *Ind. Crops Prod.*, 2024, **207**, 117752.

35 F. Zhang, Y. Liu, X. Liu, Z. Huang, J. Fu, Y. Guo and D. Song, *J. Catal.*, 2024, **436**, 115617.

36 L. S. Ribeiro, J. J. d. M. Órfão and M. F. R. Pereira, *Ind. Crops Prod.*, 2021, **166**, 113461.

37 X. Yang, X. Liu, H. Gao, C. Zhang, L. Chen and X. Liao, *Ind. Crops Prod.*, 2024, **215**, 118641.

38 J. Wang, C. Hua, X. Dong, Y. Wang and N. Zheng, *Sustainable Energy Fuels*, 2020, **4**, 1855–1862.

39 M. Gao, Z. Li, B. Zhao, S. Yu, L. Huang and Q. Wu, *Fuel Process. Technol.*, 2023, **247**, 107816.

40 W. Jia, W. Liu, Y. Cui, H. Song, C. Zhou, W. Jiang, H. Ben, X. Yang and D. Chen, *J. Catal.*, 2025, **442**, 115860.

41 D. Mullangi, V. Dhavale, S. Shalini, S. Nandi, S. Collins, T. Woo, S. Kurungot and R. Vaidhyanathan, *Adv. Energy Mater.*, 2016, **6**, 1600110.

42 X. Yu, X. Xu, L. Gao, R. Luo, Y.-F. Liu, Y.-H. Gu and S. Yuan, *Dalton Trans.*, 2024, **53**, 17902–17908.

43 Y. Nailwal, M. A. Addicoat, M. Gaurav and S. K. Pal, *ACS Appl. Nano Mater.*, 2023, **6**, 1714–1723.

44 M. Desseigne, V. Chevallier, V. Madigou, M.-V. Coulet, O. Heintz, H. Ait Ahsaine and M. Arab, *Catalysts*, 2023, **13**, 1333.

45 L. S. Ribeiro, J. Órfão, J. J. de Melo Órfão and M. F. R. Pereira, *Cellulose*, 2018, **25**, 2259–2272.

46 X. Chen, Y. Yang, Q. Xiao, X. Guo, F. Chen, X. Liu and W. Lu, *J. Mater. Sci.*, 2024, **59**, 8186–8204.

47 H. S. Xin, X. H. Hu, C. L. Cai, H. Y. Wang, C. H. Zhu, S. Li, Z. X. Xiu, X. H. Zhang, Q. Y. Liu and L. L. Ma, *Front. Chem.*, 2020, **8**, 333.

48 N. Li, X. Liu, J. Zhou, Q. Ma, M. Liu and W. Chen, *ACS Sustain. Chem. Eng.*, 2020, **8**, 9650–9659.

49 Z. Q. Xiao, Q. Zhang, T. T. Chen, X. N. Wang, Y. Fan, Q. Ge, R. Zhai, R. Sun, J. B. Ji and J. W. Mao, *Fuel*, 2018, **230**, 332–343.

50 Y. Liu, Y. Liu, Q. Wu and Y. Zhang, *Catal. Commun.*, 2019, **129**, 105731.

51 Y. Liu, Y. Liu and Y. Zhang, *Appl. Catal., B*, 2019, **242**, 100–108.

52 H. Wang, H. Xin, C. Cai, C. Zhu, Z. Xiu, Q. Liu, Y. Weng, C. Wang, X. Zhang, S. Liu, Z. Peng and L. Ma, *ACS Catal.*, 2020, **10**, 10646–10660.

53 T. T. Gao, Y. G. Sun, Y. B. Zhu, F. Lin, Y. D. Zhong, Y. Y. Li, W. X. Ji and Y. L. Ma, *New J. Chem.*, 2022, **46**, 16058–16067.

54 W. Liang, G. Xu and Y. Fu, *Appl. Catal., A*, 2025, **691**, 120052.

55 F. Goc, T. Epicier, N. Perret and F. Rataboul, *ChemCatChem*, 2023, **15**, e202201496.

56 Q. M. Wu, Q. Y. Yang, X. H. Zeng, J. H. Deng, L. Q. Zhang and J. R. Qiu, *Prog. Chem.*, 2022, **34**, 2173–2189.

57 X. Yang, Z. Li, M. Guo, T. Zhao, X. Su, W. Jiang, G. Han and H. Ben, *Fuel*, 2023, **341**, 127560.

58 T. Su, D. Wu, X. Zhang, Q. Zhang, L. Chen, X. Zhuang and L. Ma, *RSC Adv.*, 2025, **15**, 14235–14245.

59 C. Li, G. Xu, K. Li, C. Wang, Y. Zhang and Y. Fu, *Chem. Commun.*, 2019, **55**, 7663–7666.

60 Q. Xin, L. Jiang, S. Yu, S. Liu, D. Yin, L. Li, C. Xie, Q. Wu, H. Yu, Y. Liu and Y. Liu, *J. Phys. Chem. C*, 2021, **125**, 18170–18179.

61 Y. Weng, Y. Wang, M. Zhang, X. Wang, Q. Sun, S. Mu, H. Wang, M. Fan and Y. Zhang, *Catal. Today*, 2023, **407**, 89–95.

62 Y.-R. Du, B.-H. Xu, J.-S. Pan, Y.-W. Wu, X.-M. Peng, Y.-F. Wang and S.-J. Zhang, *Green Chem.*, 2019, **21**, 4792–4799.

63 M. Saito, T. Aihara, H. Miura and T. Shishido, *Catal. Today*, 2021, **375**, 64–69.

64 J. Yu, J. Liang, X. Chen, L. Wang, X. Wei, Y. Li and Y. Qin, *ACS Omega*, 2021, **6**, 11650–11659.

65 Y. Qiao, G.-J. Xia, W. Cao, K.-H. Zeng, Q.-L. Guo, X.-F. Yang, A.-Q. Wang and Y.-G. Wang, *J. Catal.*, 2023, **427**, 115114.

66 J. Song, D. Wang, Q. Wang, C. Cui and Y. Yang, *Catalysts*, 2024, **14**, 685.